

Distribution of CCS and HC₃N in L1147, an Early Phase Dark Cloud

Taiki SUZUKI¹, Masatoshi OHISHI^{1,2} and Tomoya HIROTA^{1,2}

¹ Department of Astronomical Science, the Graduate University for Advanced Studies (SOKENDAI), Osawa 2-21-1, Mitaka, Tokyo 181-8588, Japan

² National Astronomical Observatory of Japan, Osawa 2-21-1, Mitaka, Tokyo 181-8588, Japan

taiki.suzuki@nao.ac.jp

Received _____; accepted _____

CCS and HC₃N in L1147

ABSTRACT

We used the Nobeyama 45 m radio telescope to reveal spatial distributions of CCS and HC₃N in L1147, one of carbon-chain producing regions (CCPRs) candidates, where carbon-chain molecules are dominant rather than NH₃. We found that three cores (two CCS cores and one HC₃N core) exist along the NE-SW filament traced by the 850 μ m dust continuum, which are away from a Very Low Luminosity Object (VeLLO – a source that may turn into sub-stellar mass brown dwarf). The column densities of CCS are $3\text{--}7\times 10^{12}$ cm⁻² and those of HC₃N are $2\text{--}6\times 10^{12}$ cm⁻², respectively, much lower than those previously reported towards other CCPRs. We also found that two CCS peaks are displaced from that of HC₃N. In order to interpret such interleaved distributions, we conducted chemical reaction network simulations, and found that slightly different gas densities could lead to large variation of CCS-to-HC₃N ratio in the early phase of dark cloud evolution. Such a chemical “variation” may be seen in other CCPRs. Finally we were able to confirm that the L1147 filament can be regarded as a CCPR.

Subject headings: ISM: individual (L1147) — ISM: molecules — ISM: radio lines

1. Introduction

It is well known that dark cloud cores, where low mass stars are formed, can be traced by abundant carbon-chain molecules. Suzuki et al. (1992) conducted survey observations of CCS, HC₃N, HC₅N, and NH₃ toward 49 molecular clouds, and pointed out that CCS is observed in the early phase of cloud evolution, while abundance of NH₃ gradually increases in the later phase. The column density ratio of NH₃ to CCS (hereafter we call it as “NH₃/CCS” ratio) is a good indicator of cloud age, and clouds with low “NH₃/CCS” ratio are called Carbon-Chain Producing Regions (CCPRs). Such characteristics indicate that the chemical and the physical evolution of a molecular cloud are well connected, providing with useful information in investigating the cloud evolution. Since then, CCS observations were carried out to study the early phase cloud evolution. (e.g., Hirahara et al. 1992; Velusamy et al. 1995; Ohashi et al. 1999; Hirota et al. 2002, 2004; Hirota & Yamamoto 2006; Hirota et al. 2009, 2011; Taffala & Santiago 2004).

Hirota et al. (2009) carried out survey observations in order to find CCPRs outside of the Taurus region, and suggested that five molecular clouds showed lower “NH₃/CCS” ratio less than 10, which were consistent with the known features of CCPRs. Especially, four clouds, L1517D, L530D, L1147, and L1172B, showed a notable feature that their CCS column densities are lower than other CCPRs.

L1147 is a dark cloud in the Cepheus region at a distance of 325 pc (Straizys et al. 1992). Since the original Lynds’s catalog gave the same center positions for both L1147 and L1148 (Lynds 1962), some literatures call this dark cloud as L1148 (e.g., Kirk et al. (2009)). Such a situation is confusing, however, we call the source as L1147 throughout this paper since we have already adopted this source name in our past papers. Kirk et al. (2005) obtained a dust continuum map towards L1147 taken by the SCUBA at 850 μ m, and reported that the dust continuum emission is weak in this cloud, which may represent

physically young evolutionary phase. Kirk et al. (2009) also reported the dust continuum map of the entire region including L1147. They mentioned that L1147 has a Very Low Luminosity Object (VeLLO), which is defined as a source whose luminosity is lower than $0.1 L_{\odot}$, and that it may form sub-stellar mass brown dwarfs (Kauffmann et al. 2011; Di Francesco et al. 2006). This VeLLO source was discovered by the Spitzer mission, as Spitzer Multiband Imaging Photometer for Spitzer (MIPS) source, SSTc2d J204056.66+672304.9.

Among the CCPR candidates L1147 shows the lowest “NH₃/CCS” ratio of 1.5, however, Hirota et al. (2009) observed a position away from the VeLLO source. Thus further observation was needed to confirm that this dark cloud is certainly chemically young, since Hirota et al. (2009) made single point observations for the CCPR candidate sources and did not exclude a possibility that these candidate sources are located at the edge of a dense core.

In this paper, we report mapping results towards L1147 in the 45 GHz CCS and HC₃N lines, and discuss its evolutionary phase using a chemical reaction network. The observational method is described in chapter 2 (Observations); intensity distributions of CCS and HC₃N, velocity structure as well as their column density distributions are shown in chapter 3 (Results); in chapter 4 (Discussion) we will compare the CCS and HC₃N abundances with our unpublished NH₃ data and chemical reaction simulation results to discuss if L1147 is chemically young CCPR; and finally we summarize our study results in chapter 5.

2. Observations

We conducted mapping observations with the 45 m radio telescope of the Nobeyama Radio Observatory, National Astronomical Observatory of Japan, in April 2012. The CCS ($J_N=4_3-3_2$) and the HC₃N ($J=5-4$) lines in the 45 GHz region were observed simultaneously with a superconductor-insulator-superconductor (SIS) mixer receiver, whose system temperature was 200–340 K during our observations. The main beam efficiency (η_{mb}) was 0.72, and the beam size (FWHM) was 38". The pointing accuracy was checked every about two hours by observing the SiO masers ($v=1$ and 2, $J=1-0$) towards T Cep. The pointing error was estimated to be within 5". The rest frequencies, the intrinsic line strengths and the permanent dipole moments for CCS and HC₃N are $\nu = 45379.033$ and 45490.316 MHz, $S_{\text{ul}}=3.97$ and 5.00, $\mu = 2.81$ and 3.72 Debyes (Murakami 1990; Lafferty & Lovas 1978), respectively. Acousto-optical radio spectrometers with the frequency resolution of 37 kHz, corresponding to the velocity resolution of 0.24 km s⁻¹, were used for the backend. The mapping center was set to $\alpha_{2000}=20^{\text{h}}40^{\text{m}}32^{\text{s}}.0$, $\delta_{2000}=67^{\circ}21'45''$. In the mapping observations of HC₃N and CCS, the spectra were observed with a grid spacing of 40" in the position-switching mode, in which an offset position was 10' away from each source position. We observed at 39 positions along the L1147 filament (for the mapping area, see, e.g., Figure 3). The integration time per position was 200 seconds.

3. Results

3.1. Molecular Distributions

Figure 1 shows examples of the observed spectra for the individual molecules. The top panel shows the CCS spectrum at its peak ($\Delta\alpha, \Delta\delta$) = (-40", -120"), and the bottom corresponds to the HC₃N spectrum at its peak ($\Delta\alpha, \Delta\delta$) = (0", -40"), respectively. The

highest antenna temperatures were 0.89 K for CCS and 0.95 K for HC₃N, respectively, in our mapping region. Especially, in the Figure 1 (b), we could not observe the hyperfine structure ($\Delta F=0$) lines of HC₃N, suggesting that the HC₃N lines are optically thin.

Figures 2(a) and 2(b) show integrated intensity maps in the CCS $J_N=4_3-3_2$ line and HC₃N $J=5-4$ line, respectively. The velocity range of integration is from 2.3 to 3.3 km s⁻¹. We found that the CCS and HC₃N emissions are elongated in the NE–SW direction, which is consistent with the 850 μ m map obtained by Kirk et al. (2005) (see Figure 3, 850 μ m map from the SCUBA Legacy Catalogues (Di Francesco et al. 2008)). There are two CCS peaks and one HC₃N peak on the same filament: the two CCS peaks are located at (80", 0") and (-40", -120"), and one HC₃N peak is found at (0", -40"). Such the CCS distribution agrees well with the CCS $J_N=2_1-1_0$ map obtained by Kauffmann et al. (2005). Hereafter we call these three cores as “cores A, B and C”, from east to west, respectively. The line parameters in these core are summarized in Table 1. The HC₃N emission lines towards cores A and B show slightly broader linewidths due to blended hyperfine structure lines (see Figure 1(b)).

The dust continuum distribution, which would trace the H₂ density, is the strongest towards core B, followed by cores A and C. H₂ column densities were derived from the dust continuum map by using the methodology described in Kauffmann et al. (2008), assuming dust opacity is 0.01 cm² g⁻¹. **We obtained the H₂ column densities of 6.2×10^{21} cm⁻² and 1.1×10^{22} cm⁻² for cores A and B, respectively. The estimated error is 2.5×10^{21} cm⁻² in the both cores, calculated from the typical noise fluctuation of dust continuum distribution in emission-free area. Kauffmann et al. (2008) reported an estimated H₂ column density to be $7.9 \pm 0.8 \times 10^{21}$ cm⁻², which is comparable to our estimated values. However, for core C, we were able to derive a 3σ upper limit to the H₂ column density of 5.7×10^{21} cm⁻² since the**

signal-to-noise ratio was not sufficient.

The contours shown in Figures 2(a) and 2(b) show that each core would have slightly larger size than our beam of $40''$. Thus, their linear sizes would be around 0.07 pc or more, considering the distance of 325 pc. In Figure 2(b) the contours around cores B and C are interconnected. This might mean that the two cores correspond to substructures within a single core.

The VeLLO source (SSTc2d J204056.66+672304.9) is shown as a black star in Figures 2(a) and 2(b). Prior to the mapping observations we expected to reveal a core in the vicinity of the VeLLO source since a protostellar core is often associated with an infrared source. However, we did not see a prominent core near the VeLLO source.

Channel maps of CCS and HC_3N are shown in Figures 4(a) and 4(b). From Figure 4(a) it is possible to mention that the two CCS cores have slightly different V_{LSR} values; the core C has the V_{LSR} value of 2.8–3.3 km s^{-1} , while the core A has a slightly blue-shifted value. Further the core C appears as a more prominent core than the core A. In Figure 4(b) only the core B is visible, which has wider line width, and V_{LSR} is 2.3–3.5 km s^{-1} and is slightly extends along the NE–SW ridge. No major HC_3N peak corresponds to the cores A and C, however, it is seen that HC_3N emission exists at around the two CCS peaks. Detailed descriptions for individual cores are summarized in Table 1.

In our mapping observations, we found that the three peaks are clearly interleaved to each other, contrary to the past observation results where CCS and HC_3N show similar spatial distributions (Hirahara et al. 1992; Tafalla et al. 2006; Hirota et al. 2002, 2004). For example, Figure 4 in Hirota et al.(2009) showed the integrated intensity maps of CCS and HC_3N towards seven dark clouds. The spatial distributions of CCS and HC_3N in six dark clouds are very similar, including their peak positions, even if there is a slight difference in the distributions. Only one exception is L1172D: there are two CCS peaks and

a HC₃N is located between the CCS peaks. It is well known that carbon-chain molecules are sometimes depleted in the central part of an infrared source and that their distributions show a central hole (Velusamy et al. 1995; Kuiper et al. 1996; Ohashi et al. 1999; Lai & Crutcher 2000; Lai et al. 2003). The observed characteristics of the interleaved peaks seem to have different spatial distributions from the “central-hole” case mentioned above, and we will discuss later how such the interleaved distribution could be explained.

3.2. Position-Velocity Maps

Figure 5 shows position-velocity maps in L1147. For CCS, we have put a cutting line (a–a’) along the edge passing through the cores A and C. Additionally we have set two cutting lines perpendicular to the line a–a’, passing through these cores. We drew four lines in Figure 5 (a) and (b), including three cores (b–b’ and c–c’). Similarly for HC₃N, we have set a cutting line (d–d’) perpendicular to the line (a–a’) and passing through the core B. The position velocity maps along the ridge (bottom left in Figure 5) and perpendicular to the cores (bottom right in Figure 5) do not show any sign of rotation. This fact would be consistent with that the three cores are in an very early phase in their physical evolution.

3.3. Molecular Column Densities

We derived the column densities of CCS and HC₃N. For the calculations, we used the following equations with assuming the local thermal equilibrium (LTE) condition and that the both lines are optically thin:

$$T_A^* = \eta_{mb}[J(T_{ex}) - J(T_{BB})][1 - \exp(-\tau)] \quad (1)$$

where

$$J(T) = (h\nu/k)[\exp(h\nu/kT) - 1]^{-1}, \quad (2)$$

$$N = \frac{3h}{8\pi^3} \frac{Q}{\mu^2 S_{ij}} \Delta v \frac{\exp(E_u/kT_{\text{ex}})}{\exp(h\nu/kT_{\text{ex}}) - 1} \tau \quad (3)$$

In these equations, η_{mb} denotes the main beam efficiency, ν the rest frequency of the line, N the column density, Δv the line width (FWHM), Q the rotational partition function, S_{ij} the intrinsic line strength of the transition, μ the permanent dipole moment, E_u the upper state energy from the ground state rotational level. Since we observed a single line for each molecule, the excitation temperatures were fixed to 5 K for CCS and 6.5 K for HC₃N, which are consistent with our previous studies (e.g., Suzuki et al. 1992; Hirota et al. 2009). A change of excitation temperature by 1 K makes a change of their column densities about 30%.

Figure 6 shows derived column density distributions along the prominent NE–SW ridge seen in the integrated intensity maps (Figure 2). The column densities of the both molecules resulted in a range of $2\text{--}7 \times 10^{12} \text{ cm}^{-2}$, which is consistent with the values reported by Hirota et al. (2009). We have found that the derived column densities of CCS ($3\text{--}7 \times 10^{12} \text{ cm}^{-2}$) are less by about one order of magnitude than those in other known CCPRs, e.g., $66 \times 10^{12} \text{ cm}^{-2}$ for TMC1(CP) (Suzuki et al. 1992) and $53 \times 10^{12} \text{ cm}^{-2}$ for L492 (Hirota et al. 2009).

The three peaks (cores A, B and C) are also seen in the column density distributions along the NE–SW ridge, however, we have found that the column density ratio between CCS and HC₃N (hereafter called as “CCS/HC₃N” ratio) varies dramatically. We summarized in Table 2 their column densities, fractional abundances relative to H₂, and “CCS/HC₃N” ratios. The errors of column densities are calculated by using the r.m.s noise in each observation. The upper limit to the column density of HC₃N in core C was calculated using the 3σ r.m.s noise at this position. We have taken the estimated error of H₂ into account when calculating the fractional abundance values. **Note that the dust emission in core C is weaker than the noise level. Therefore we used 3 σ level of r.m.s noise for**

H₂ density to calculate the upper limit of the fractional abundances of CCS.

In core A, CCS has higher abundance than that of HC₃N. On the other hand this trend is reversed in core B, as revealed in their column density ratio. Especially, core C, where HC₃N was not seen, has an extremely high CCS abundance; we are able to indicate only the lower limit to the abundance ratio. **Since both the H₂ and HC₃N column densities are given as lower limits, we were not able to estimate the fractional abundance of HC₃N toward core C.**

4. Discussion

In this section we will discuss if L1147 can be regarded as a CCPR, and how we could reconcile the displacement of emission peaks and the variation in the CCS-to-HC₃N ratio among the prominent cores.

4.1. NH₃ Data in the L1147 Filament

The first issue that we want to clarify is if L1147 is a CCPR as a whole. In this regard, it would be important to know how strong or weak the NH₃ line is. Hirota et al. (2009) reported the NH₃ (1,1) data only towards the (0'', -80'') position by using the Nobeyama 45m radio telescope, which shows very weak emission (the antenna temperature of 80 mK). Hirota et al. (2013) **observed the NH₃ (1,1) line towards the IRS position (the VeLLO source), however, the line was too faint to detect with an r.m.s. noise level of 30 mK.** Therefore it is possible to calculate an upper limit to the column density of NH₃ towards the VeLLO source with the same method used by Hirota et al. (2009), which is $9 \times 10^{12} \text{ cm}^{-2}$. This value is comparable with that reported by (Hirota et al. 2009) ($8 \times 10^{12} \text{ cm}^{-2}$). Since the beam size is large (~ 80 arcseconds), the two beams

covered the most part of the mapping area in the CCS and the HC₃N lines. Thus we may conclude that the column density of NH₃ in the L1147 filament is less than $9 \times 10^{12} \text{ cm}^{-2}$ as a whole. When we use this upper limit to the NH₃ column density together with the column densities of CCS tabulated in Table 2, the “NH₃/CCS” ratio is found in a range between 0.95 and 4.3. This leads us to confirm that the entire L1147 filament is a CCPR.

4.2. Variation of “CCS/HC₃N” Ratios

It is well known that abundances of carbon-chain molecules increase rapidly then decrease as the cloud evolves (Suzuki et al. 1992). Although Suzuki et al. (1992) reported observation results for CCS, HC₃N, HC₅N and NH₃, they did not compare abundances of CCS and HC₃N based on their gas-phase chemical evolution model. Further, at the best of our knowledge, no one has conducted such comparisons, especially in the early phase of cloud evolution. The “CCS/HC₃N” ratio is expected to be uniform since cores formed in a single filament would have similar evolutionary phase. However, we have found that the three cores in the L1147 filament show different the variation of “CCS/HC₃N” ratios. This would suggest that the three cores are in different evolutionary phases.

Then can we see such variations of the “CCS/HC₃N” ratio for other dark clouds ? Figure 7 shows a **cloud-to-cloud variation** of the “CCS/HC₃N” ratio as a function of the “NH₃/CCS” ratio. The data were taken from Suzuki et al. (1992) and Hirota et al. (2009) where the CCS, HC₃N and NH₃ data are available. Since it is well known that the “NH₃/CCS” ratio is a good indicator of chemical evolution of a cloud, this plot represents a time-evolution of the “CCS/HC₃N” ratio along with the chemical evolution. A **weak** trend can be seen from this figure that a majority of cores in the CCPRs and their candidates (the “NH₃/CCS” ratio is less than 10) have higher “CCS/HC₃N” ratio whereas a majority of evolved cores have lower “CCS/HC₃N” ratio.

In order to understand difference of the three cores in L1147 as well as the trend of the “CCS/HC₃N” ratios, it would be a methodology to utilize chemical reaction network simulations for understanding chemical evolution of early phase molecular clouds.

4.3. Chemical Evolution Model

We have conducted chemical evolution simulations based on a latest theoretical model that incorporates surface reactions on the dust particles.

For chemical reactions and their rate coefficients, we used the KIDA (KInetic Database for Astrochemistry) dataset (Wakelam et al. 2012), which is a collection of measured and theoretical values published in literatures. The simulation code was also provided by Wakelam et al. (2012), and includes 684 molecules and 8317 reactions. The simulation code numerically solves the chemical kinetics equations, shown below, that describes the formation and destruction of molecules.

$$\frac{dn_i}{dt} = \sum_{l,m} k_{lm} n_l n_m - n_i \sum_{i \neq l} k_l n_l + k_i^{\text{des}} n_i^s - k_i^{\text{acc}} n_i \quad (4)$$

$$\frac{dn_i^s}{dt} = \sum_{l,m} k_{lm}^s n_l^s n_m^s - n_i^s \sum_{i \neq l} k_l^s n_l^s + k_i^{\text{des}} n_i^s - k_i^{\text{acc}} n_i \quad (5)$$

where n_i and n_i^s are the gas-phase and surface concentrations of the i -th species (cm^{-3}), k_{lm} and k_l are the gas-phase reaction rates (in units of s^{-1} for the first-order kinetics and $\text{cm}^3 \text{s}^{-1}$ for the second-order kinetics), k_i^{acc} and k_i^{des} denote the accretion and desorption rates (s^{-1}), and k_{lm}^s and k_l^s are the surface reaction rates ($\text{cm}^3 \text{s}^{-1}$). It should be noted that this model assumes a constant number density of hydrogen atom and other physical parameters throughout a simulation. The gas kinetic temperature was fixed to 10 K, a typical value for a dark cloud, and the visual extinction, A_v , was fixed to 10 magnitudes. As the initial

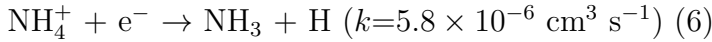
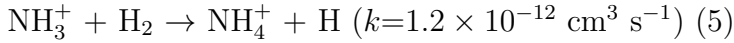
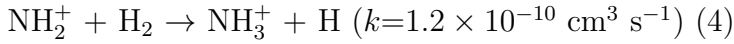
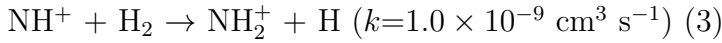
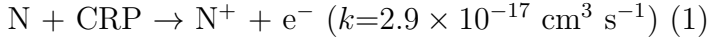
elemental abundances (see Table 3, we adopted the EA2 set used by Wakelam & Herbst (2008)).

Figure 8 shows examples of our simulation results for the H density of 1×10^4 , 2×10^4 , and $6 \times 10^4 \text{ cm}^{-3}$. The gray region corresponds to the observed column density range for CCS and HC_3N . As can be seen from Figure 8, CCS is produced rapidly in the early phase (less than 10^5 years) of the cloud evolution and decrease afterward. On the other hand, N-bearing species (HC_3N , HC_5N and NH_3) increase gradually. Although HC_3N and HC_5N decrease along with the decrease of CCS, NH_3 increases monotonically in the whole evolution. Such a behavior is similar to that reported and discussed in Suzuki et al. (1992).

Such behavior of their abundance is well connected with the formation process. The formation process of CCS was discussed in Suzuki et al. (1992); the neutral carbon (C) would play an important role for the production of CCS. As a cloud evolves, C^+ is converted into C, and finally into CO in the later phase. CCS production is efficiently produced in the early phase of cloud evolution, and its fractional abundance is highest around 10^4 - 10^5 years, where the C atom shows its highest abundance among C^+ , C and CO.

HC_3N , another carbon-chain molecule, also reaches to the maximum in the same time range. Regarding its formation process, it was suggested that a neutral-neutral reaction between C_2H_2 and CN would be important (Fukuzawa et al. 1998), which has no reaction barrier. C_2H_2 is produced in relatively early phase of cloud evolution, while CN formation would longer time. CN can be formed via $\text{CH} + \text{N}^+$ and/or $\text{NH} + \text{C}$. As described in the formation of NH_3 below, these reactions are related to the ionization of N atom, which takes longer time. As a result, HC_3N starts to increase a bit later than CCS in our simulations. Both of CCS and HC_3N abundances decrease dramatically in the later phase of cloud evolution, because most of C atoms are converted into CO, and the formation of carbon-chain molecules is no longer efficient.

On the other hands, the fractional abundance of NH_3 shows very different behavior. Laboratory experiments showed solid-phase reaction to form NH_3 would not be efficient, and most of NH_3 would be formed in the gas-phase (Hiraoka et al. 2006). In our simulation, it is assumed that only atomic nitrogen exist initially. The formation of NH_3 would be initiated by the ionization of N by a cosmic ray particle (CRP). Then sequential reactions with H_2 (Herbst & Kelemperer 1973) form NH_4^+ . Finally, NH_3 is produced through recombination of NH_4^+ with electron. We summarize a series of reactions together with their rate coefficients k at 10 K in the brackets.



Reaction (2) has a small rate coefficient since it has an activation energy of about 42 K. Although reaction (5) has a “negative” activation energy of about -36 K, the prefactor is so small ($3.36 \times 10^{-14} \text{ cm}^3 \text{ s}^{-1}$). Such small rate coefficients, including the ionization of N atom by a cosmic ray, would result in long time in forming NH_3 . We drew a vertical line at 10^5 years in Figure 8, corresponding to a typical age for dark clouds. The observed column densities of CCS and HC_3N agree with the simulation results within a factor of 10 ($X_{\text{obs}}/10 \leq X_{\text{model}} \leq 10X_{\text{obs}}$) where X_{obs} is the observed abundance and X_{model} is the model abundance. The same criterion is also used by experts in chemical reaction network simulations, (e.g., Wakelam & Herbst 2008). We find that our simulated column densities tend to be always higher than our observation results, and it would not be suitable to

compare directly by means of individual column densities. However, we found that the ratio of CCS to HC₃N was roughly matched with the past observations of CCPRs. Thus, in the following section, we will use the ratio of CCS to HC₃N when comparing our observed results and simulated ones. Furthermore, we can ignore the uncertainty of hydrogen column density by using their ratios.

4.4. Comparison between Observational and Simulation Results

We simulated chemical evolution under different densities from 10^4 to 10^6 cm⁻³, and compared “CCS/HC₃N” ratio with our observation between 3.16×10^4 and 1.0×10^7 years. Some examples of simulation under different densities are shown in Figures 8(b) and (c). It is seen that chemical evolution would be accelerated in physically evolved denser cores due to larger number of reactants per unit volume.

Figures 9(a), (b), and (c) show the simulated “CCS/HC₃N” ratios derived in different densities and ages. Each figure has the same ratio value for the same age and the density, but we prepared three ones to compare simulation with the individual three cores since they have the different fractional abundance of CCS and HC₃N, and the “CCS/HC₃N” ratio. We compared Figure 9 (a) with core A, (b) with core B, and (c) with core C. Now we classify them in terms of the observed ratios. As we expected, NH₃ becomes dominant in the later phase compared with carbon-chain molecules. Since NH₃ is so weak in L1147, such an evolutionary stage would not be appropriate for L1147. Thus we excluded them in our comparison (in Figure 9 the regions are shown in grey). Some regions painted in white are not suitable in terms of the “CCS/HC₃N” ratios. We also excluded regions where observed fractional abundances of CCS and HC₃N are not within a factor of 10 (the regions are shown in purple and blue). **For Core C, we did not use the fractional abundance of HC₃N as criteria of comparison since we were only able to set upper limits to**

the column density of HC₃N and H₂. Then we found that the observed “CCS/HC₃N” ratios in cores A, B and C can be reproduced in orange regions between 6×10^4 – 1×10^6 years, typical for dark clouds in Figures 9 (a)–(c). All appropriate regions are those just before NH₃ becomes dominant. In realistic dark clouds, physical evolution would be accelerated along with the increase of gas density.

4.5. Evolutionary Phases in the Cores

In this last subsection we would like to discuss if the three cores were formed and evolved in a similar way.

Figures 9 (a)–(c) were made assuming the visual extinction of 10 magnitude. Core C is located in the edge of the L1147 filament where the gas density could be lower than those in cores A and B, and could have a lower visual extinction. Figure 9 (d) represents the result of a simulation with the visual extinction of 7.5 magnitude. Our simulations suggested that carbon-chain molecules tend to decrease more slowly in the later phase. This trend would conflict with the fact that HC₃N was not observed in the core C. As shown in Figure 9 (d), we could not find the appropriate region that explain observed column density with this parameter.

On the other hand we were able to reproduce the chemical properties in cores A and B in the appropriate evolutionary phase for dark clouds (around 1×10^5 years). Our results suggest that these cores may have slightly different densities which might have lead to slightly different evolutionary phases and subsequently a little different chemical properties. Such a slight density difference might be achievable by enhancing a very small density fluctuation through gravitational instabilities even if the L1147 filament was formed at a given time.

While the chemical properties in the core C was reproduced in a lower density using the same visual extinction with core A and B, we could not find the suitable region assuming lower visual extinction. This would mean that an improvement of the model is required to better explain the chemical properties in the core C. In any case it was found that a combination of observational studies and chemical reaction network simulations can provide with a powerful means in investigating chemical evolution of molecular clouds. We would like to stress that the simulation code as well as the reaction databases are available online, and any researchers are able to utilize this powerful tool.

Finally, although there should be a density profile in a core and the density will increase in the actual cloud evolution, our model assumed constant hydrogen density. Thus it would be needed to develop the chemical reaction network simulation code to incorporate more realistic physical evolution of a cloud in order to better understand the chemical evolution of a molecular cloud.

In the present study, we had to assume the excitation temperatures because we conducted single line observations. Such observational constraint could introduce some uncertainties to our results. Future multi-line observations would be needed to discuss the chemical differences in the early phase of cloud evolution in more detail.

5. Conclusions

The main results of this paper can be summarized as follows.

1. It was confirmed that the L1147 cloud is a CCPR by combining the new CCS mapping result and past NH_3 observational results by Hirota et al. (2009).
2. Two CCS cores and a HC_3N core were found in the L1147. Three peaks are away from the Spitzer source (VeLLO source) and are located interleaved to each other.

Such a different spatial distributions between CCS and HC₃N have not been known except for only one dark cloud (1172D).

3. The column densities of CCS are $3\text{--}7 \times 10^{12} \text{ cm}^{-2}$ and those of HC₃N are $2\text{--}6 \times 10^{12} \text{ cm}^{-2}$, respectively, which are much lower than those reported in other CCPRs. In the three cores detected in L1147, the column densities are different within a factor of a few. We found that the “CCS/HC₃N” ratios in the three cores are different despite that they are formed in the same filament.
4. We used the chemical reaction network model to discuss if we can reproduce the “CCS/HC₃N” ratios derived in our observations assuming different densities from 10^4 cm^{-3} to 10^6 cm^{-3} . We found that our results can be reproduced for $6 \times 10^4\text{--}6 \times 10^5$ years; such a time range is typical for dark cloud cores and would be appropriate for CCPRs. It would be likely that the difference of the “CCS/HC₃N” ratios in L1147 is explained by slightly different H₂ density. L1147 would be in physically and chemically early phase of a cloud evolution, and our result suggests a possibility that chemical features in the early phase may change among cores with different physical conditions. On the other hands, core C is not reproduced in our simulation under realistic visual extinction. Further development of the chemical model would be required.

6. Acknowledgements

We are grateful all the staff members of Nobeyama Radio Observatory, the National Astronomical Observatory of Japan (NAOJ), for their support throughout our observations. We thank to Dr. J. M. Kirk for consulting with our questions regarding the SCUBA map, to Drs. V. Wakelam and Y. Aikawa for providing us with the KIDA data and the chemical reaction simulation code, and to the anonymous referee who provided us with

many valuable comments.. A part of the data analysis was made at the Astronomy Data Center, NAOJ. We utilized the Japanese Virtual Observatory (<http://jvo.nao.ac.jp/>) in finding the SCUBA 850 μm data.

REFERENCES

- Benson, P. J., & Myers, P. C., *ApJS*, 71, 89 (1989).
- Di Francesco, J., Evans, II, N. J., Caselli, P., et al., in *Protostars & Planets V*, 17 (2007).
- Di Francesco, J., Johnstone, D., Kirk, H., MacKenzie, T., & Ledwosinska, E., *ApJS*, 175, 277 (2008).
- Fukuzawa K., Osamura Y., Schaefer H. F. III, *ApJ*, 505, 278 (1998).
- Herbst, E. & Kelemperer, W., *ApJ*, 185, 505 (1973).
- Hirahara, Y., et al., *ApJ*, 394, 539 (1992).
- Hiraoka, K., Mochizuki, N., & Wada, A. *API Conf. Proc.* 855, 86 (2006).
- Hirota, T., Ito, T., & Yamamoto, S., *ApJ*, 565, 359 (2002).
- Hirota, T., Maezawa, H., & Yamamoto, S., *ApJ*, 617, 399 (2004).
- Hirota, T., Ohishi, M. & Yamamoto, S., *ApJ*, 699, 585 (2009).
- Hirota, T., Sakai, T., Sakai, N., & Yamamoto, S., *ApJ*, 736, 4 (2011).
- Hirota, T., et al., unpublished (2013).
- Hirota, T., & Yamamoto, S., *ApJ*, 646, 258 (2006).
- Kauffmann, J., Bertoldi, F., Bourke, T. L., Evans II, N. J., & Lee, C. W., *A&A*, 487, 993 (2008).
- Kauffmann, J., Bertoldi, F., & Evans II, N. J., *AN*, 326, 878 (2005).
- Kauffmann, J. et al., *MNRAS*, 416, 2341 (2011).

- Kirk, J. M., Ward-Thompson, D., & André, P., *MNRAS*, 360, 1506 (2005).
- Kirk, J. M., Ward-Thompson, D., Di Francesco, J., et al., *ApJS*, 185, 198 (2009).
- Kuiper, T. B. H., Langer, W. D., & Velusamy, T., *ApJ*, 468, 761 (1996).
- Lafferty, W. J., & Lovas, F. J., *J. Phys. Chem. Ref. Data*, 7, 441 (1978).
- Lai, S.-P., & Crutcher, R. M., *ApJS*, 128, 271 (2000).
- Lai, S.-P., Velusamy, T., Langer, W. D., & Kuiper, T. B. H., *AJ*, 126, 311 (2003).
- Lynds, B. T., *ApJS*, 7, 1 (1962).
- Murakami, A., *ApJ*, 357, 288 (1990).
- Ohashi, N., Lee, S. W., Wilner, D. J., & Hayashi, M., *ApJ*, 518, L41 (1999).
- Scott, G. B. I., Freeman, C. G., & McEwan, M. J., *MNRAS*, 290, 636 (1997).
- Straizys, V., Cernis, K., Kazlauskas, A., Meistas, E., *Baltic Astron.*, 1, 149 (1992).
- Suzuki, H., Yamamoto, S., Ohishi, M., Kaifu, N., Ishikawa, S., Hirahara, Y., & Takano, S.,
ApJ, 392, 551 (1992).
- Tafalla, M., & Santiago, J., *A&A*, 414, L53 (2004).
- Tafalla, M., Santiago-García, J., Myers, P. C., Caselli, P., Walmsley, C. M., & Crapsi, A.,
A&A, 455, 577 (2006).
- Velusamy, T., Kuiper, T. B. H., & Langer, W. D., *ApJ*, 451, L75 (1995).
- Wakelam, V.; KIDA Team., *EAS*, 58, 287 (2012).
- Wakelam, V., & Herbst, E., *ApJ*, 680, 371 (2008).

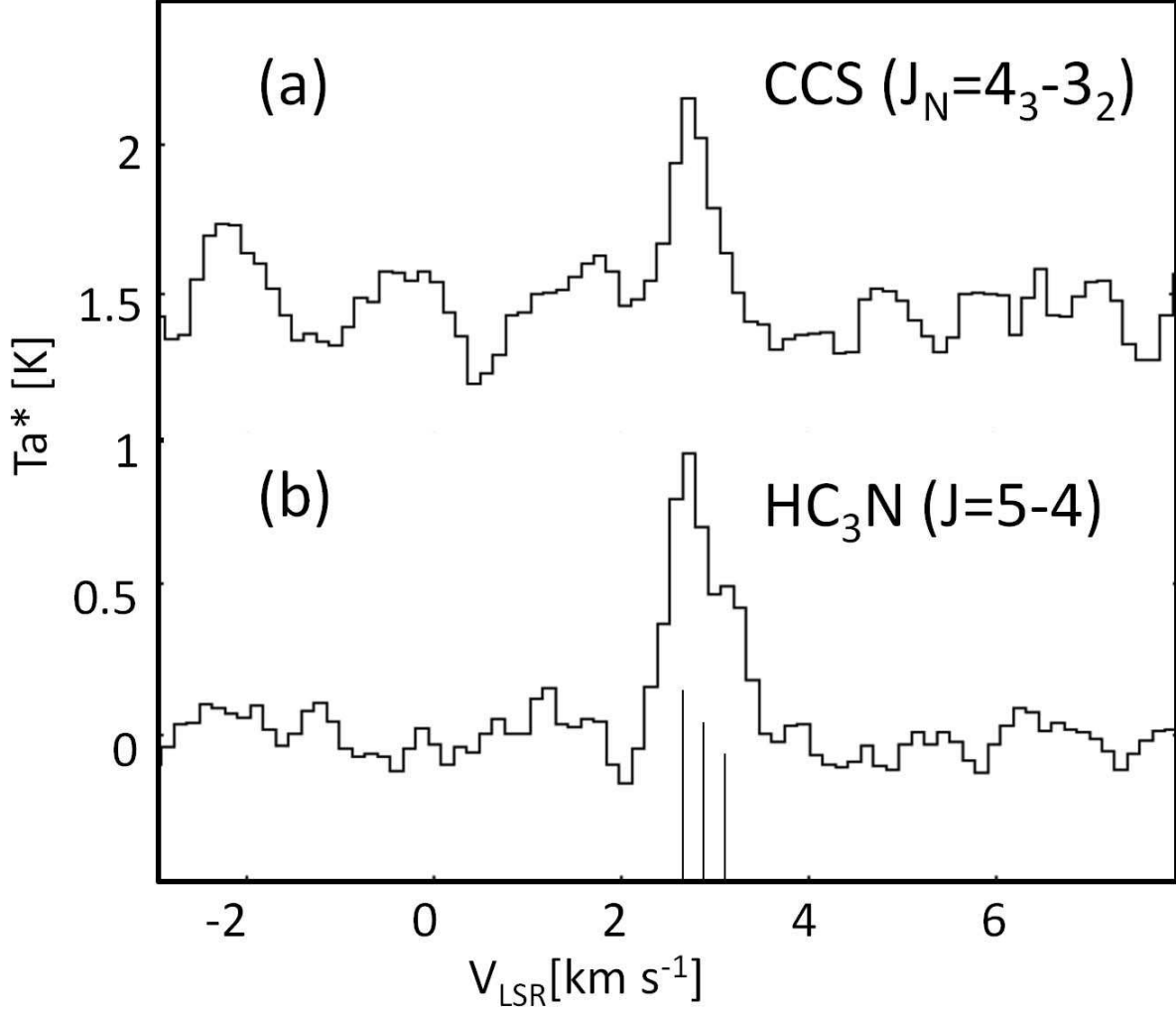


Fig. 1.— Sample spectra of the (a) CCS ($J_N=4_3-3_2$) at $(\Delta\alpha, \Delta\delta)=(-40'', -120'')$ and (b) HC₃N ($J=5-4$) at $(\Delta\alpha, \Delta\delta)=(0'', -40'')$. The HC₃N line has a broader linewidth due to partially resolved three main ($\Delta F=1$) hyperfine structure lines, whose theoretical locations and intensity pattern are shown at the bottom of the figure. Note that two weaker ($\Delta F=0$) hyperfine structure lines are located outside of this figure. **Note that the temperature scale for the CCS line is offset by 1.5 K.**

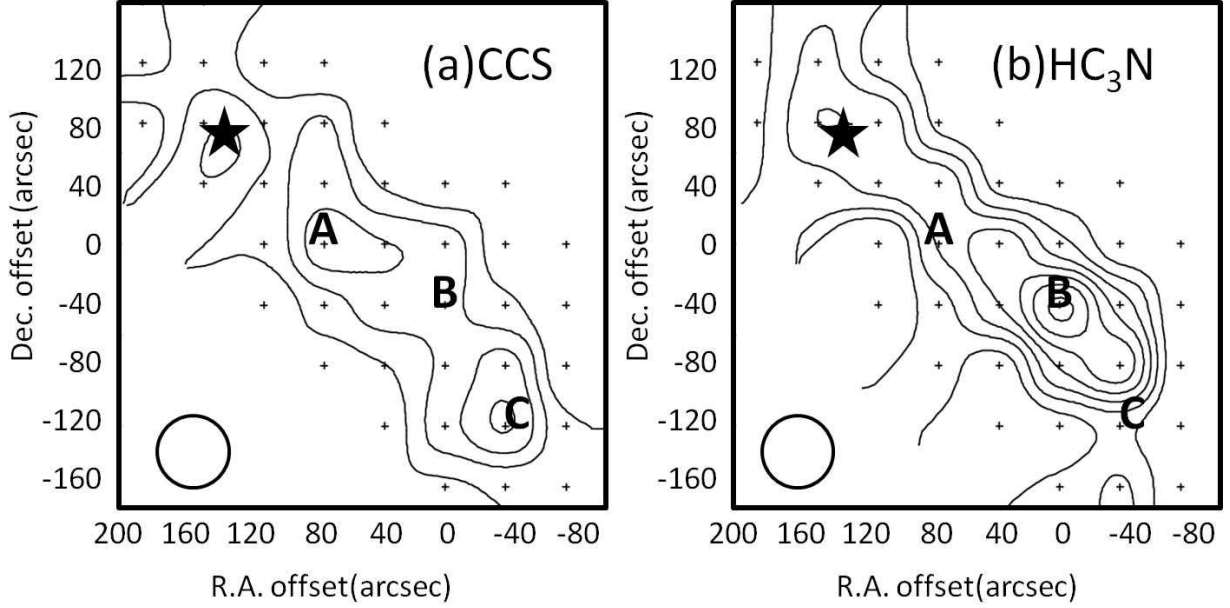


Fig. 2.— Integrated intensity maps of the observed molecules towards L1147. The reference position is $\alpha_{2000}=20^{\text{h}}40^{\text{m}}32^{\text{s}}.0$, $\delta_{2000}=67^{\circ}21'45''$. The mapping positions are shown by the cross marks which trace a filamentary area seen in the dust continuum map in Figure 3. The Spitzer point source (SSTc2d J204056.66+672304.9) is shown by the black star. The beam size is shown at the lower left corner. (a) CCS ($J_N=4_3-3_2$): the velocity range of integration is from 2.3 to 3.3 km s^{-1} . The contour interval is 0.07 K km s^{-1} , and the lowest contour level is 0.05 K km s^{-1} . (b) HC_3N ($J=5-4$): the velocity range of integration is from 2.3 to 3.3 km s^{-1} . The contour interval is 0.07 K km s^{-1} , and the lowest contour level is 0.05 K km s^{-1} . Three prominent cores are indicated as A–C.

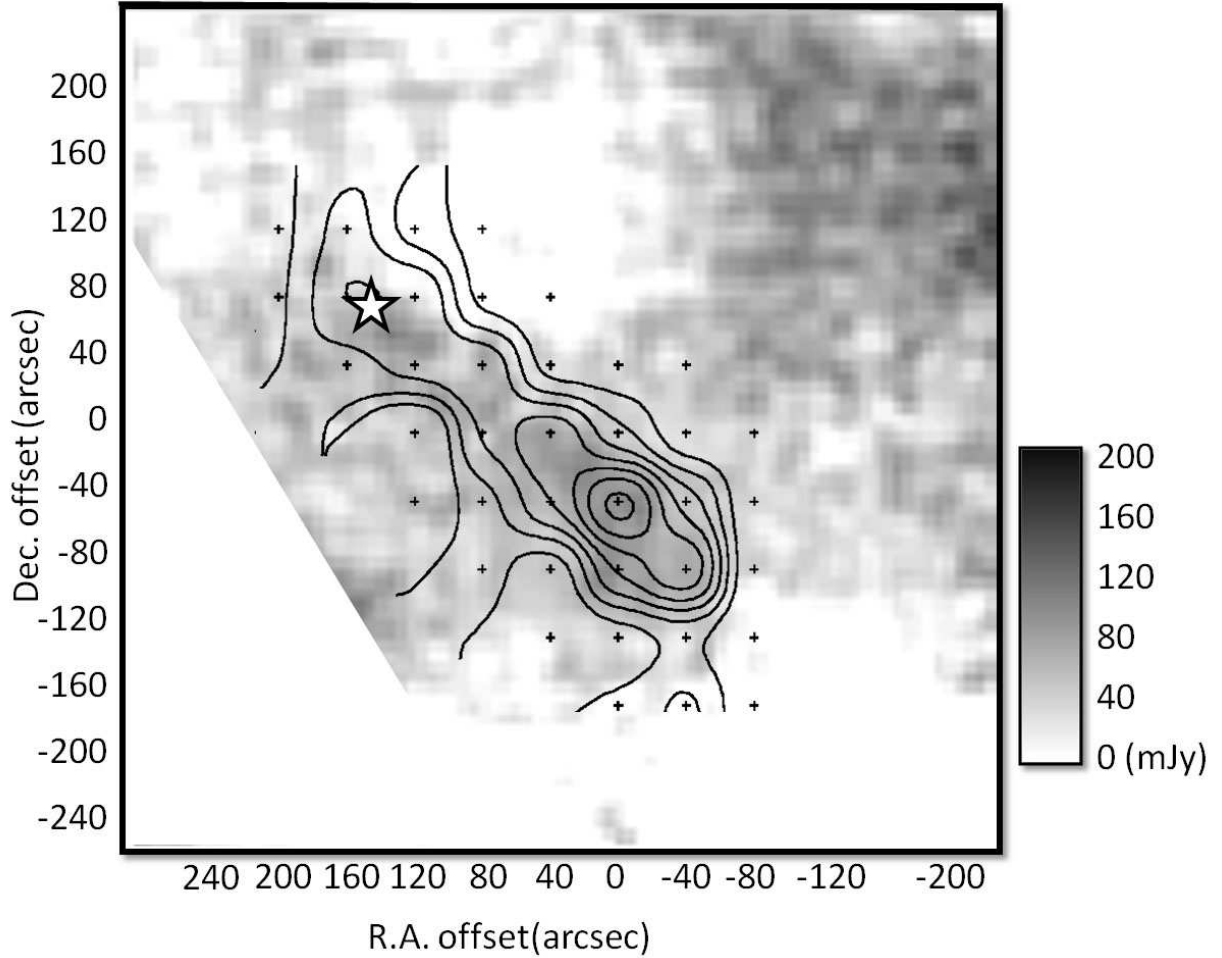


Fig. 3.— The dust continuum map obtained by SCUBA (Kirk et al. 2005). Dust continuum distribution is elongated toward NE–SW direction as shown in gray scale. Integrated intensity map of HC_3N is superposed. This trend matches well with CCS and HC_3N distribution. Our observation positions are denoted by the “+” marks.

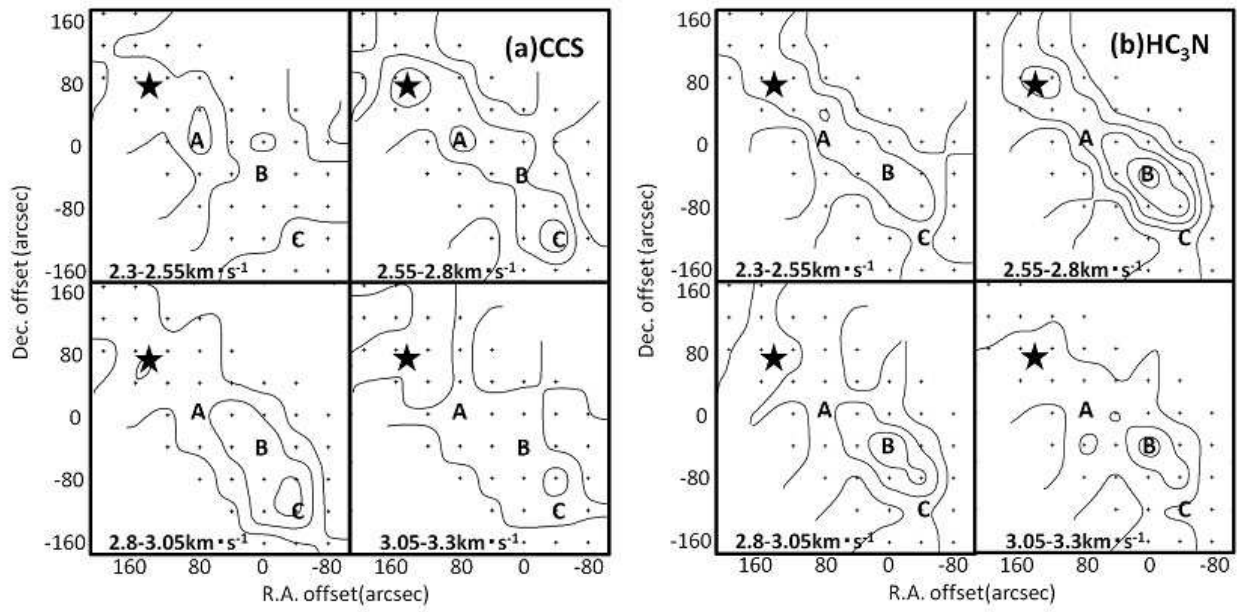


Fig. 4.— The channel maps of (a) CCS and (b) HC_3N . The contour interval is 0.04 K km s^{-1} and the minimum contour value is 0.01 K km s^{-1} for both species. The mapping region is the same as in Figure 2.

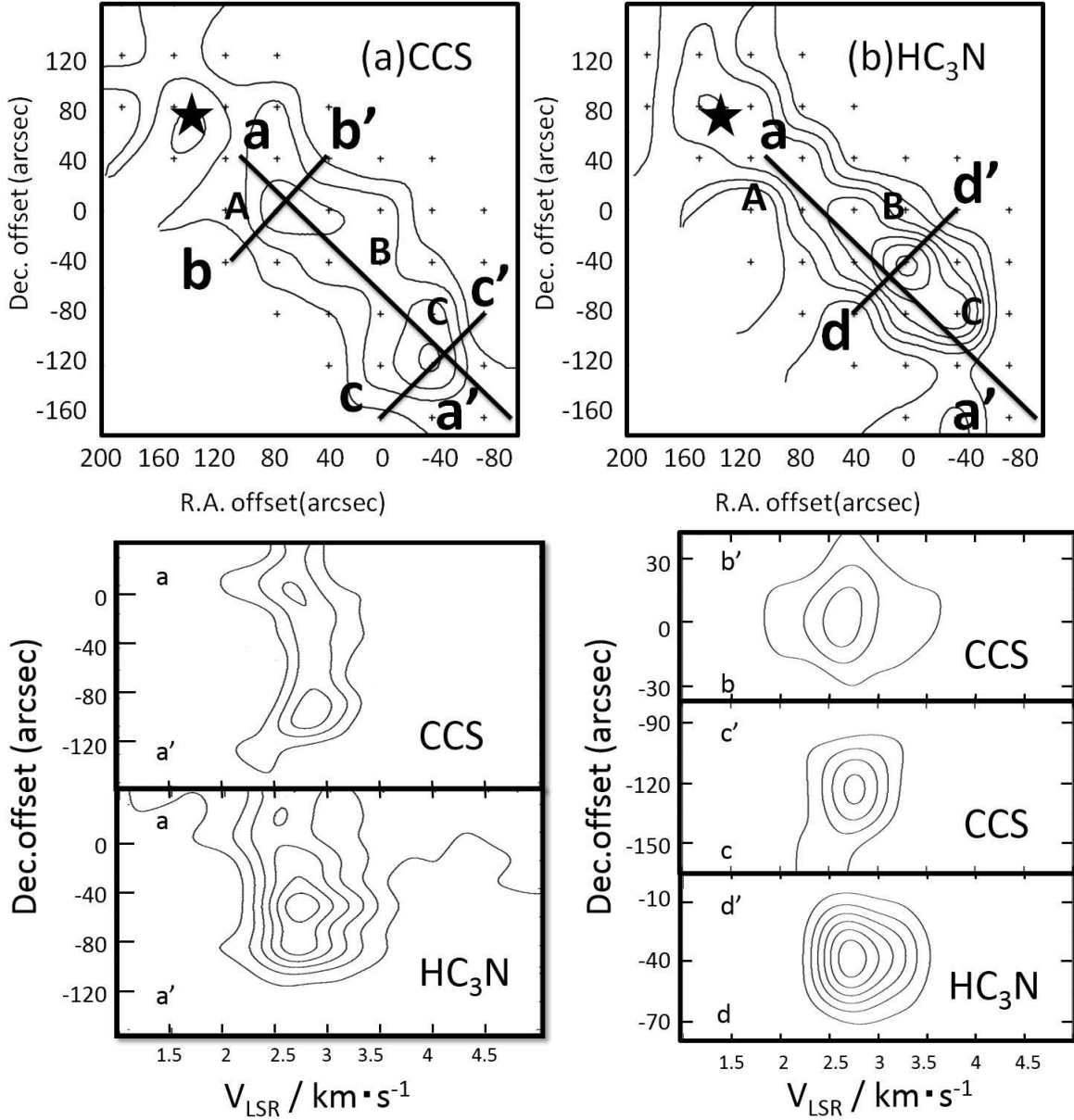


Fig. 5.— Position-velocity maps of the CCS $J_N=4_3 - 3_2$ and HC₃N $J = 5 - 4$ lines. The cutting lines are shown in the upper integrated maps, as (a–a’), common cutting both in CCS and HC₃N maps, (b–b’), (c–c’), and (d–d’). The contour interval is 0.1 K km s⁻¹, and the lowest contour level is 0.07 K km s⁻¹. Three prominent cores are indicated as A–C, as is the case for Figure 2. Lower figures show position-velocity maps along each cutting line.

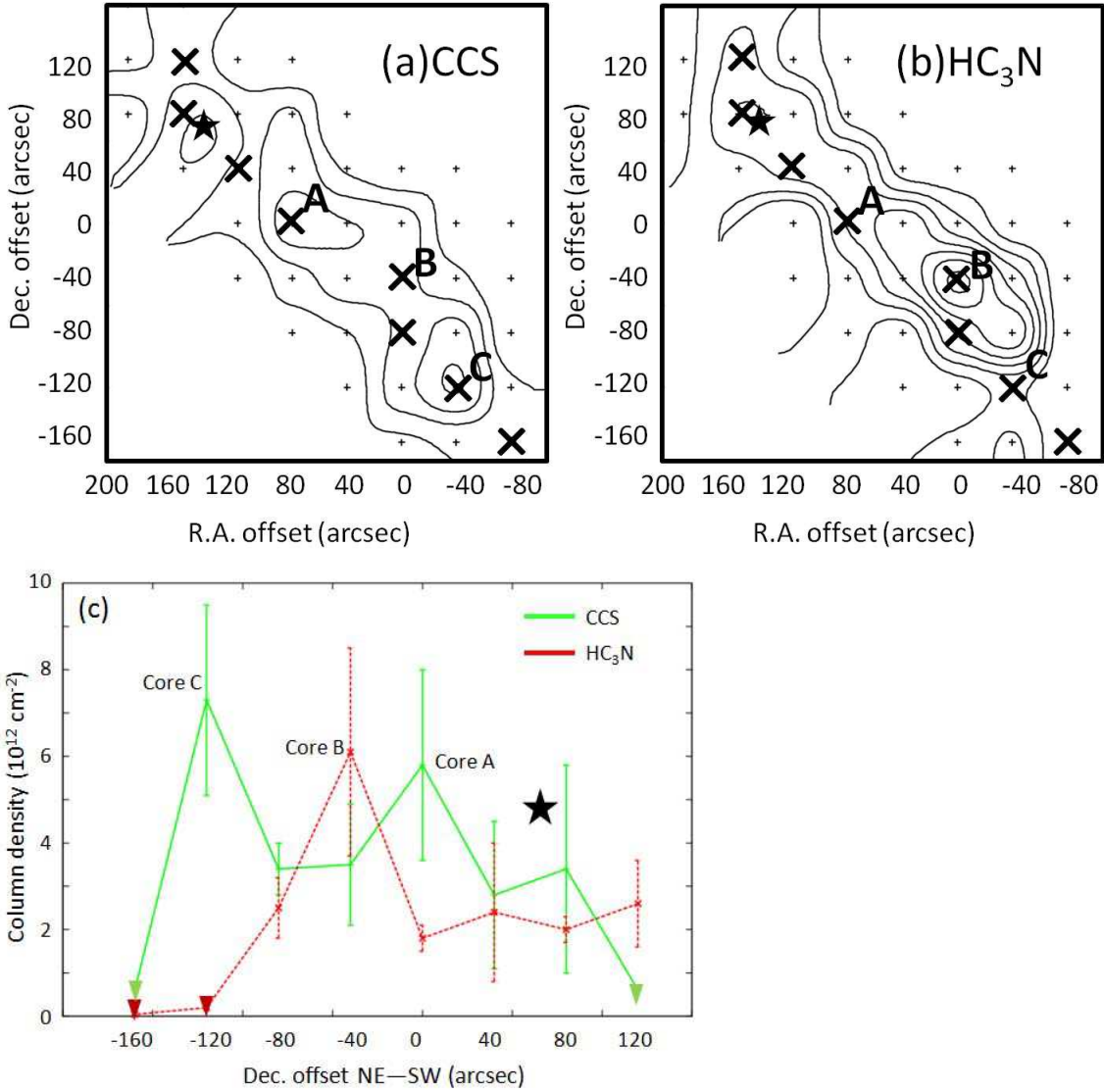


Fig. 6.— (a) and (b) We have chosen eight points along the ridge with different declination offsets; (c) Distribution of column densities of CCS and HC₃N along the ridge. The abscissa denotes the declination offset, whose positions are shown in (a) and (b). The position of the VeLLO source is shown by the black star.

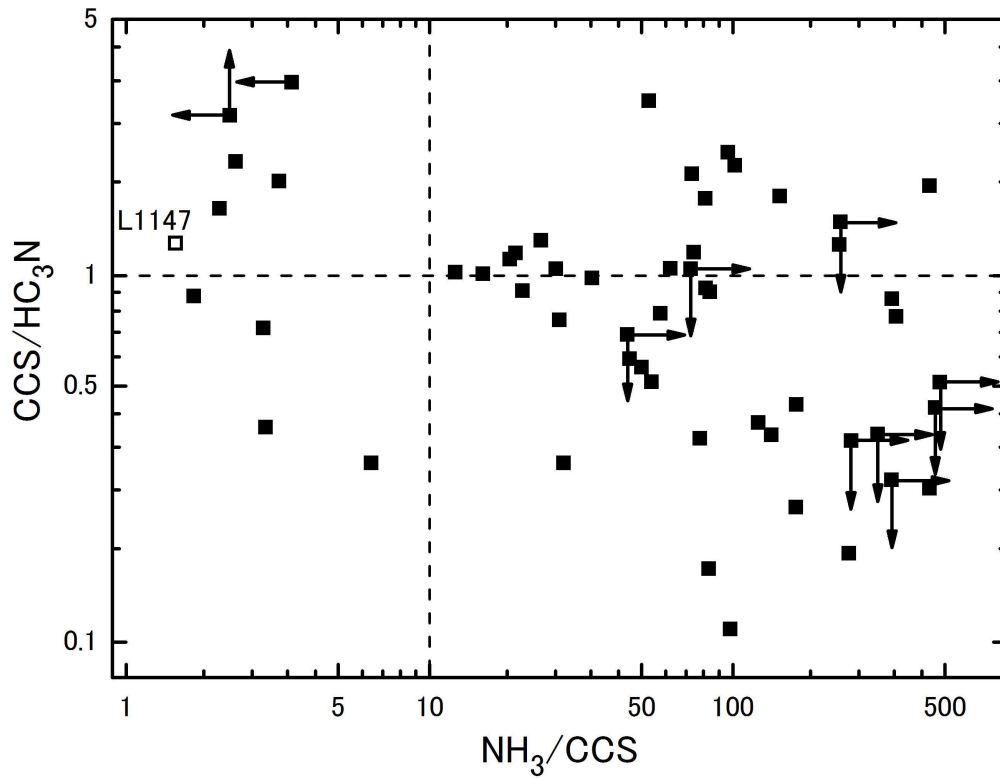


Fig. 7.— “ $\text{CCS}/\text{HC}_3\text{N}$ ” ratio as a function of “ NH_3/CCS ” ratio in various clouds. The data points were taken from Suzuki et al. (1992) and Hirota et al. (2009) where the CCS, HC_3N and NH_3 data are available. The arrows indicate upper or lower limits to the ratios. The data point corresponding to L1147 is shown in the open square.

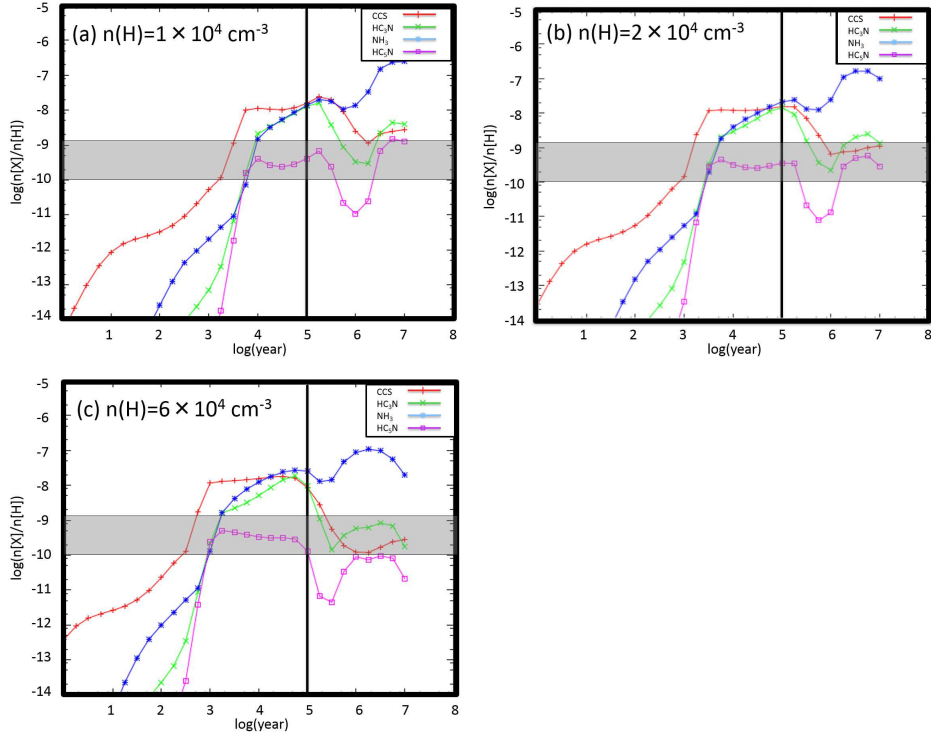


Fig. 8.— Examples of simulation results for different hydrogen number densities: (a) $1 \times 10^4 \text{ cm}^{-3}$, (b) $2 \times 10^4 \text{ cm}^{-3}$, and (c) $6 \times 10^4 \text{ cm}^{-3}$. Vertical line denotes 1×10^5 years, a typical age of a dark cloud core. The column density range for CCS and HC₃N derived in our observation is shown in the gray region.

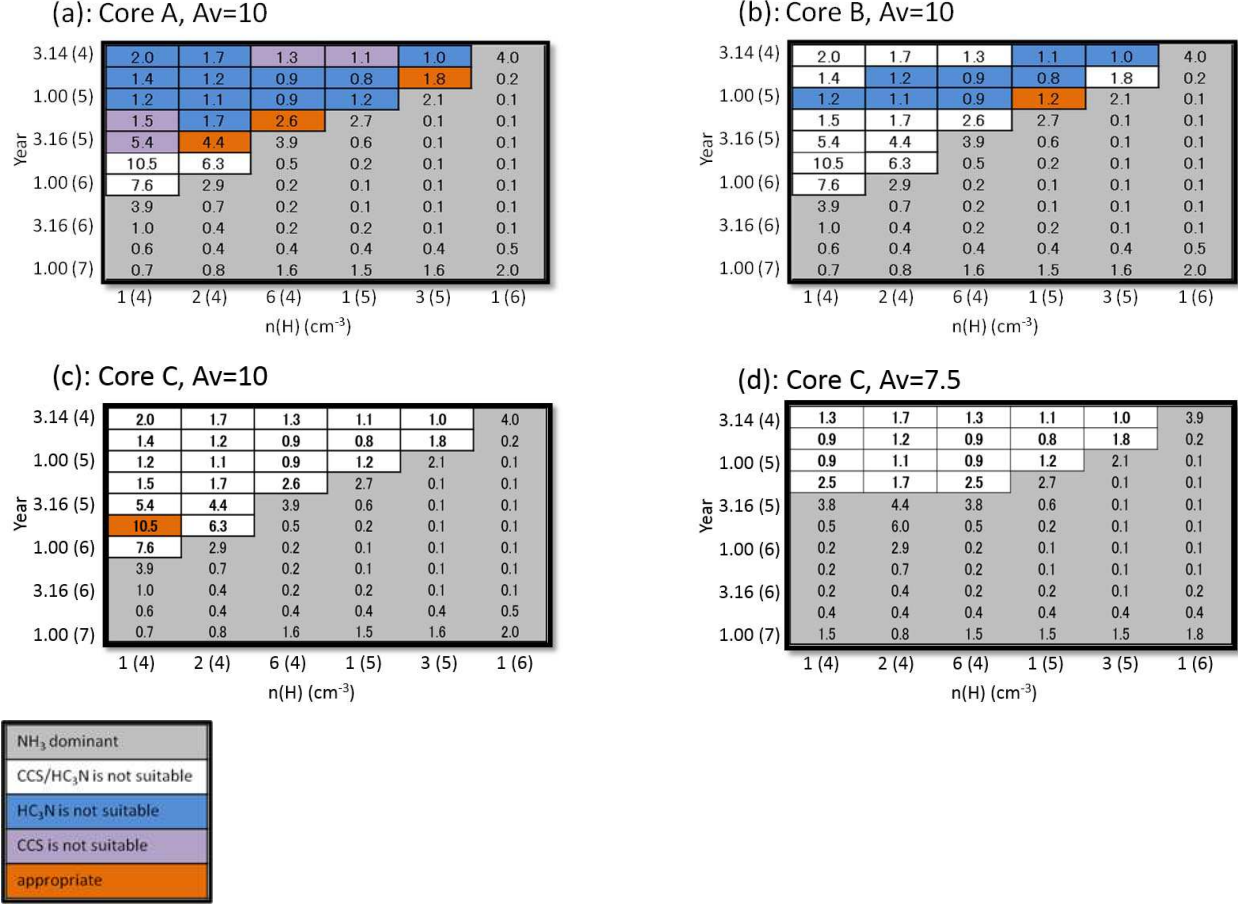


Fig. 9.— “CCS/HC₃N” ratio derived in our simulation for different times and hydrogen number densities. In the figures, time and density are represented in $\alpha(\beta)$ which means $\alpha \times 10^\beta$. We classify their values using different colors. Grey regions corresponds to NH₃ dominant phase, white ones show unsuitable “CCS/HC₃N” ratios, and blue and purple ones show too much HC₃N and CCS abundance. **For Core C, where the fractional abundance of HC₃N was not determined, we took into account fractional abundances of NH₃ and CCS and the “CCS/HC₃N” only.** Appropriate ratios and column densities are achieved in the orange region. (a), (b), and (c) represent comparison with cores A, B, and C, respectively. Visual extinction is fixed to be 10 magnitude in (a)-(c). For (d) we used the visual extinction to 7.5 magnitude, since it corresponds to the core C which would be a lower gas density region at an edge of the L1147 filament.

Table 1. Observed Line Characteristics towards Cores A, B, and C

core	CCS ($J_N=4_3-3_4$)				HC ₃ N ($J=5-4$)			
	T_B (rms) (K)	V_{LSR} (km s ⁻¹)	Δv (km s ⁻¹)	$\int T_B dv$ (3σ) (K km s ⁻¹)	T_B (rms) (K)	V_{LSR} (km s ⁻¹)	Δv (km s ⁻¹)	$\int T_B dv$ (3σ) (K km s ⁻¹)
A	0.72 (0.10)	2.6	0.5	0.38 (0.16)	0.49 (0.09)	2.4	0.5	0.26 (0.14)
B	0.63 (0.10)	2.8	0.6	0.40 (0.19)	0.95 (0.08)	2.7	0.7	0.71 (0.18)
C	0.89 (0.10)	2.7	0.5	0.47 (0.16)	<0.21 (0.07)	–	–	<0.13

Table 2. Column Densities, Fractional abundances, and CCS/HC₃N Ratios towards Cores A, B, and C

core	N[CCS] (10 ¹² cm ⁻²)	N[HC ₃ N] (10 ¹² cm ⁻²)	N[H ₂] (10 ²¹ cm ⁻²)	X[CCS] (10 ⁻¹⁰)	X[HC ₃ N] (10 ⁻¹⁰)	N[CCS]/N[HC ₃ N]
A	5.8 (\pm 3.9)	1.8 (\pm 0.9)	6.2 (\pm 1.9)	9.5 (\pm 7.1)	3.0 (\pm 1.7)	3.2 (\pm 2.6)
B	3.5 (\pm 2.5)	6.1 (\pm 4.3)	11 (\pm 1.9)	3.3 (\pm 2.4)	5.7 (\pm 4.1)	0.6 (\pm 0.6)
C	7.4 (\pm 4.3)	<0.8	<5.7	>13	-	>9

Table 3. Initial Elemental Abundances

Element	Abundance	Element	Abundance
He	9.00(-2)	Fe ⁺	2.00(-7)
N	7.60(-5)	Na ⁺	2.00(-7)
O	2.56(-4)	Mg ⁺	2.40(-6)
C ⁺	1.20(-4)	Cl ⁺	1.8(-7)
S ⁺	1.50(-5)	P ⁺	1.17(-7)
Si ⁺	1.70(-6)	F ⁺	1.8(-8)

Note. — Elemental abundance used in our chemical reaction model. This table is referred from Wakelam & Herbst (2008).